PERFORMANCE OF NUMERICAL WEATHER PRODUCTS FOR INSAR TROPOSPHERIC CORRECTION: A CASE STUDY OF A TROPICAL REGION

Pius Kirui[a,b,*], Björn Riedel[a], Markus Gerke[a]

[a] Institute of Geodesy and Photogrammetry Bienroder weg 81, 38106 Braunschweig, Germany
p.kirui@tu-braunschweig.de
[b]Department of Geomatic Engineering, Jomo Kenyatta University of Agriculture and Technology, Nairobi, Kenya

Commission 111, WG 111/3

KEY WORDS: Tropospheric delay, numerical weather models, Sentinel-1, InSAR

ABSTRACT:

Tropospheric delay variability remains a significant source of error in the InSAR-derived measurements. Numerical weather models have been proposed as an alternative technique to mitigate tropospheric delays in InSAR and have become a standard procedure for some multi-temporal InSAR processing workflows. This study evaluates the viability of three numerical weather models for mitigating tropospheric delay in InSAR for a tropical region. We assess their performance in correcting tropospheric delay in Sentinel-1 interferograms at different spatial wavelengths using variograms. Their performance is validated using GNSS tropospheric delay and our proposed SAR-derived tropospheric delay estimates. The results indicate that numerical weather model estimates do not mitigate short-wavelength turbulent delays, but can mitigate long-wavelength stratified delays to some extent, which may also introduce additional errors in interferograms. At a spatial wavelength of 40 km, 36% of the interferograms showed increased spatial autocorrelation after correction with GACOS, 55% with ERA-5, and 51% with MERRA-2. In contrast the InSAR-derived tropospheric delays resulted in a significant reduction in variance at all wavelengths indicating the ability to mitigate both turbulent and stratified delays. Our study demonstrates the limited potential of numerical weather model estimates to satisfactorily mitigate trophospheric noise in InSAR and the capability of InSAR-derived trophospheric delay to significantly correct tropospheric noise in InSAR.

1. INTRODUCTION

InSAR as a geodetic tool has facilitated deformation monitoring globally and provides insights into fields related to anthropogenic activities (Amelung et al., 1999, Castellazzi et al., 2016), geophysical processes (Furuya and Satyabala, 2008, Elliott et al., 2010), and landslides (Ye et al., 2004, Zhang et al., 2018). Despite the progress made in InSAR related to data availability and processing algorithms, InSAR, like any other space-based radio technique, still faces the challenge of atmospheric delay modelling (Murray et al., 2019). Atmospheric noise results from the interaction of the radio signal with the ionosphere and troposphere which causes phase advance and phase delay, respectively. The influence of the ionosphere is insignificant for short-wavelength satellite-based SAR such as Sentinel-1 C-band data and can be ignored (Fattahi et al., 2017, Liang et al., 2019). [1]

The mitigation of tropospheric noise in InSAR has a significant effect on the reliability of InSAR-derived measurements, and ignoring tropospheric noise could lead to the misreporting of tropospheric delays as deformation (Yip et al., 2019, Hamling and Kilgour, 2021). In conventional multi-temporal InSAR (MTI) processing, tropospheric noise is mitigated by applying a low-pass spatial filter and high-pass temporal filter, assuming spatially correlated noise and random correlation over time (Ferretti et al., 2001). Other alternative methods have also been proposed to correct tropospheric noise in InSAR owing to the limitations of time-series filtering. The correction methods include the use of external datasets to estimate tropospheric delay from external data, such as GNSS, spectrometers, and numerical weather models (NWM).

The use of numerical weather models estimates to correct tropospheric noise in InSAR is gaining popularity because of their global coverage and freely available data which have continuously improved in resolution. Moreover, some MTI processing software such as STAMPS (Hooper et al., 2012), MintPy (Yunjun et al., 2019), OSARIS (Loibl et al., 2019), and LICSBAS (Morishita et al., 2020) have integrated NWM as a standard step in the MTI processing chain. The corrections are ingested either directly utilizing GACOS (Yu et al., 2018) or standalone packages such as Python based Atmospheric Phase Screen estimation(PyAPS) (Jolivet et al., 2014) and The Toolbox for Reducing Atmospheric InSAR Noise(TRAIN) (Bekaert et al., 2015). The success rates of NWM in correcting tropospheric noise in InSAR have been inconsistent, with different studies reporting conflicting accuracies attributed to the coarse resolution of NWM, different climatic zones, complex topography, and rapidly changing tropospheric conditions (Foster et al., 2013, Stephens et al., 2020). Additionally, the performance of numerical weather models is still unknown in regions such as Africa, which are characterized by limited data used to initialize numerical weather models (Shen et al., 2019). The lack of performance metrics is also attributed to the few InSAR studies conducted in these regions. For instance, Kenya, based on Scopus search, has only five published studies. Hence, evaluating the potential of numerical weather models to account for tropospheric noise in InSAR in these regions is essential because InSAR applications will grow given the open-source software and global availability of Sentinel-1 data.

* Corresponding author

We, therefore, in this paper evaluate the performance of three recent numerical weather model outputs in mitigating the short-wavelength turbulent and long-wavelength stratified delay in Sentinel-1 interferograms along the Kenyan Rift. The Kenyan Rift is characterized by complex terrain and its floor consists of a series of volcanoes and lakes that cause local variability in the troposphere. The 6-day or 12-day Sentinel-1 revisit times facilitate the direct estimation of SAR-based tropospheric delay. We use the interferometric relationship of the phase components to empirically estimate the tropospheric delay from InSAR. The tropospheric delay from the numerical weather models is validated using estimated SAR-based and GNSS-derived tropospheric delays. We quantify the performance of numerical weather models ability to reduce spatial phase variability in short-interval interferograms that is attributed to tropospheric delay differences.

2. METHOD

2.1 Study area and Data

This study is conducted in the southern section of the Kenya Rift Valley. We utilize 60 Sentinel-1 images acquired in Interferometric Wide (IW) swath mode from ascending orbit path 130 for the period 2018-2020. We process data from the most recent global numerical weather models, including the ERA-5 reanalysis from European Centre for Medium-Range Weather Forecasts (ECMWF), Modern-Era Retrospective Analysis for Research and Applications Version 2 (MERRA-2) from NASA and the High RESolution (HRES) from the ECMWF. The resolutions of the weather products are presented in table 1. We also process GNSS data to validate tropospheric delay estimates from two GNSS stations as shown in figure 1.

Table 1. Numerical weather models data characteristics.

Model	Spatial resolution	Temporal resolution
ERA-5	31 km x 31 km	1 hour
MERRA-2	55 km × 68 km	6 hours
HRES ECMWF	12.5 km × 12.5 km	6 hours

2.2 Numerical weather models

The tropospheric phase delay as the radar signal is transmitted is a function of air refractivity, N, and constitutes both hydrostatic and wet delays. The hydrostatic tropospheric delay is less variable and constitutes 90 per cent of the delay, whereas the wet delay is small but highly variable (Hanssen, 2001).

$$\Delta_{\text{tropo}} = 10^{-6} \int N(h)dh = k_1 \frac{P_d}{T} + k_2 \frac{e}{T} + k_3 \frac{e}{T^2} \quad (1)$$

where k_1, k_2, and k_3 are the constants as defined by (Smith and Weintraub, 1953), P_d is the surface pressure, T the temperature, e is the partial pressure of water vapour.

We estimate the tropospheric delay from ERA-5 and MERRA-2 numerical weather model data using TRAIN (Bekaert et al., 2015). It is estimated by integrating equation 1 along the signal line of sight as

$$\Delta_{\text{tropo}} = \frac{10^{-6}}{cos\theta} \int_h^{h_{ref}} (N_{hydro} + N_{wet})dh \quad (2)$$

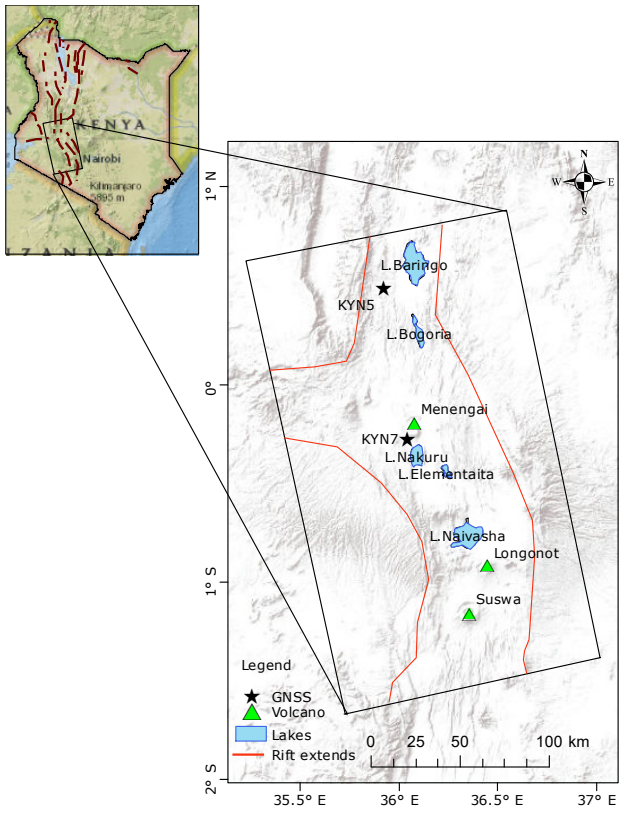

Figure 1. Map showing the study area, location of volcanoes, lakes, and the two GNSS stations KYN5 and KYN7 from the Uganda-Kenya Eastern Branch GNSS Network.

where h is the surface elevation, and h_{ref} is the top of the tropospheric column. The pseudo-range tropospheric delay is then converted into a phase delay, as follows:

$$\phi_{trop} = \frac{-4\pi}{\lambda} \Delta_{\text{tropo}} \quad (3)$$

where θ indicates the incidence angle and λ the radar wavelength.

The tropospheric delay is already estimated and provided as total tropospheric delay for HRES data via the Generic Atmospheric Correction Online Service (GACOS) (Yu et al., 2018). GACOS combines HRES data and continuous GNSS tropospheric delay estimates with 5-minute intervals by applying an iterative tropospheric decomposition model (Yu et al., 2017) that fits the exponential function to estimate the stratified delay and modified inverse distance weighted model.

2.3 SAR Tropospheric delay

A 6-day or 12-day Sentinel-1 unwrapped interferogram that has been corrected for spatial look-angle error is composed of tropospheric delay, deformation component, and processing errors.

$$\theta_{unw} = \theta_{def} + \theta_{tropo} + \theta_{noise} \quad (4)$$

where θ_{unw} is the unwrapped phase and θ_{def}, θ_{atm} and θ_{noise} are the deformation, tropospheric delay, and processing noise components. The short revisit time makes the deformation component negligible. The deformation or tropospheric delay components can be eliminated using a linear combination of interferograms that share a common image (Hanssen, 2001). We

eliminate the deformation phase component in short-interval interferograms by subtracting the interferograms that share a common image as shown in equation 5.

$$\theta_{tropo_{1,2,3}} = \theta_{unw_{1,2}} - \theta_{unw_{2,3}} = 2x_2 - x_1 - x_3 \quad (5)$$

where $\theta_{tropo_{1,2,3}}$ is the tropospheric delay for the three SAR acquisitions, x_1 is the tropospheric delay in the first acquisition, x_2 is the tropospheric delay in the shared SAR and x_3 is the delay in the third acquisition.

Using equation 5 we generate linearly combined interferograms corresponding to each SAR acquisition. The linearly combined double-differenced interferograms contain unknown tropospheric delay components and processing errors. This combination results in an ill-posed linear adjustment problem because of the lack of independent observations owing to the differencing of neighboring observations. We solve the ill-posed linear problem using Tikhonov regularization which seeks to derive estimates closest to the actual values by adding a regularization parameter to the objective function (Golub et al., 1999). The estimates are then solved by minimizing the objective function. In ("Multi-temporal InSAR tropospheric delay modelling using Tikhonov regularization for Sentinel-1 C-band data" submitted) this approach is described in detail and experiments confirm its superiority compared to other existing approaches.

2.4 GNSS Tropospheric delay

We estimate the GNSS tropospheric delay by using GAMIT (Herring et al., 2010). We use the average of the estimated GNSS delays 30 minutes before and after the SAR acquisition time to obtain the tropospheric delay corresponding to SAR acquisition. The tropospheric delay is referenced to the GNSS station KYN7, which acts as a reference station for NWM-based tropospheric delay and estimated SAR-based tropospheric delay. The GNSS pseudorange tropospheric delay is converted to a phase delay using equation 3.

2.5 InSAR Processing

The InSAR Scientific Computing Environment(ISCE) (Rosen et al., 2018) is used to generate a stack of co-registered SLC (Fattahi et al., 2016). The stacked SLC are preprocessed for SBAS-MTI processing in STAMPS (Hooper et al., 2012). We generate interferograms with a maximum temporal baseline of 48 days and a maximum geometric baseline of 300m. Scatters with amplitude dispersion difference of lower than 0.6 are selected as potential persistent scatterers candidates ensuring enough number are selected while at the same time reducing the size of the selected data. The scatterers are further selected based on their temporal coherence which is an indicator of phase stability and corrected for spatially correlated terms through bandpass filtering in the frequency domain. The spatially uncorrelated look angle error is corrected using the correlation between phase and the geometrical baseline. The interferograms are unwrapped using the 3D minimum cost flow method. We correct tropospheric delay influence in the interferograms using the procedures described in sections 2.2 and 2.3.

3. RESULTS AND DISCUSSION

3.1 Tropospheric delay estimates

Equation 5 provides means of directly comparing the ability of different tropospheric delay estimates to replicate the tropospheric delay difference in InSAR. It is expected that the predictive models will have similar spatial variability with the original tropospheric delay corresponding to the three acquisitions because the deformation component is eliminated through the linear combination of the interferograms. However, significant differences are observed between the NWM-based tropospheric delay estimates and original tropospheric delay estimates. For instance, the phase variability in the northeast of the double-diffrenced interferogram is not captured by the three NWM-based estimates. Similarly, MERRA-2 fails to capture the phase variability in the southern section of the interferogram , as shown in figure 2.

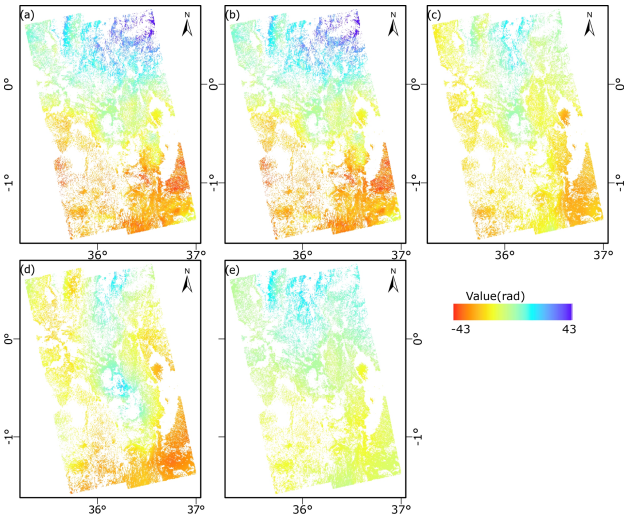

Figure 2. Estimates of tropospheric delay for three SAR acquisition dates, 2018-01-26, 2018-02-07, and 2018-02-19, based on equation 5. (a) displays the original interferogram-based estimates, while (b) depicts the SAR-based estimates, whereas (c), (d), and (e) display the tropospheric delay estimates from GACOS, ERA-5, and MERRA-2, respectively.

The inability of NWM-based tropospheric estimates to replicate tropospheric delay is further demonstrated using short-interval interferograms, in which the phase variability is attributed to the tropospheric delay difference in between SAR acquisitions in absence of rapid large-amplitude deformation. We observe a consistent spatial pattern between the original short-interval interferograms and estimated SAR-based differential delays. In contrast, we observe instances where significant differences existed between the NWM-based differential delay and original short-interval interferograms. In addition, the three numerical weather model estimates exhibited varying spatial variability, as shown in figure 3.

In addition, we observe a strong influence of elevation in the NWM-based tropospheric delay estimates even when the tropospheric noise in the interferogram do not correlate with elevation, as shown in figure 4. We also noted a minimal change in variability of tropospheric delay at an elevation range of 3500m-4000m compared to the lower elevation ranges. The correlation between the NWM-based tropospheric estimates is attributed to the integral formula in equation 1 that assumes that the tropospheric delay variability is based entirely on the elevation difference. Therefore, NWM-based tropospheric delay estimates fail to capture tropospheric delay variability in the presence of a strong turbulent delay. Although GACOS has been shown to

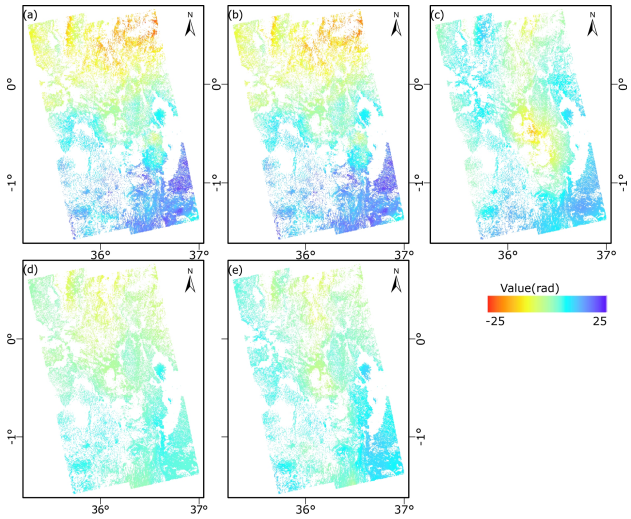

Figure 3. Evaluation of the spatial variability between the original short-interval interferogram and differential tropospheric delay estimates. The interferogram (a) is the original unwrapped interferogram (20180102_20180114), (b) is the corresponding SAR-based differential delay, while (c), (d), and (e) correspond to ERA-5, GACOS, and MERRA-2 differential delays, respectively.

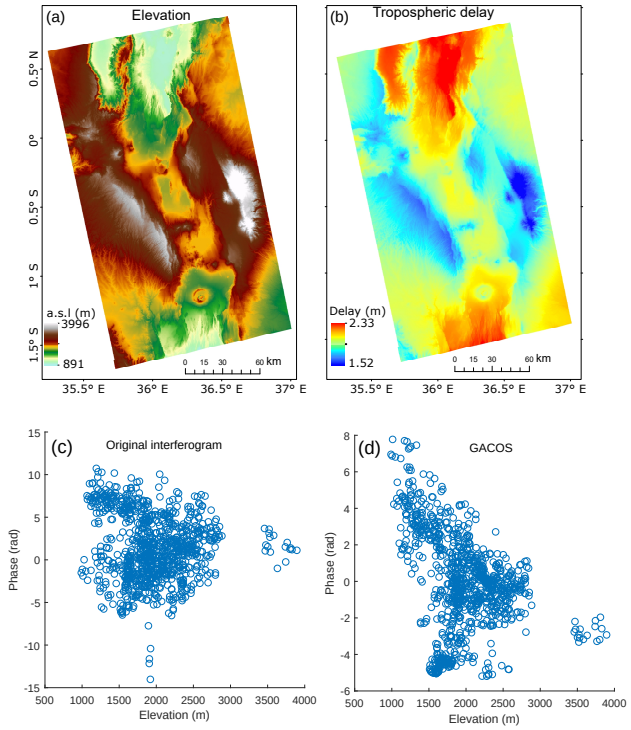

Figure 4. A comparison of correlation between elevation (a) and GACOS differential tropospheric delay and the correlation between elevation and unwrapped phase. (c) shows the correlation between the original interferogram (20180303-20180315) and elevation while (d) is the correlation between corresponding GACOS differential delay and elevation.

estimate turbulent tropospheric delay to some extent, it fails to account for local variability in our case study region owing to the lack of sufficient GNSS points to estimate the constraint of the turbulent delay.

3.2 Validation of tropospheric delay estimates

We observed a mixed pattern in the temporal fit between the NWM-based tropospheric delay and the GNSS tropospheric delay. There were days on which the discrepancy between the

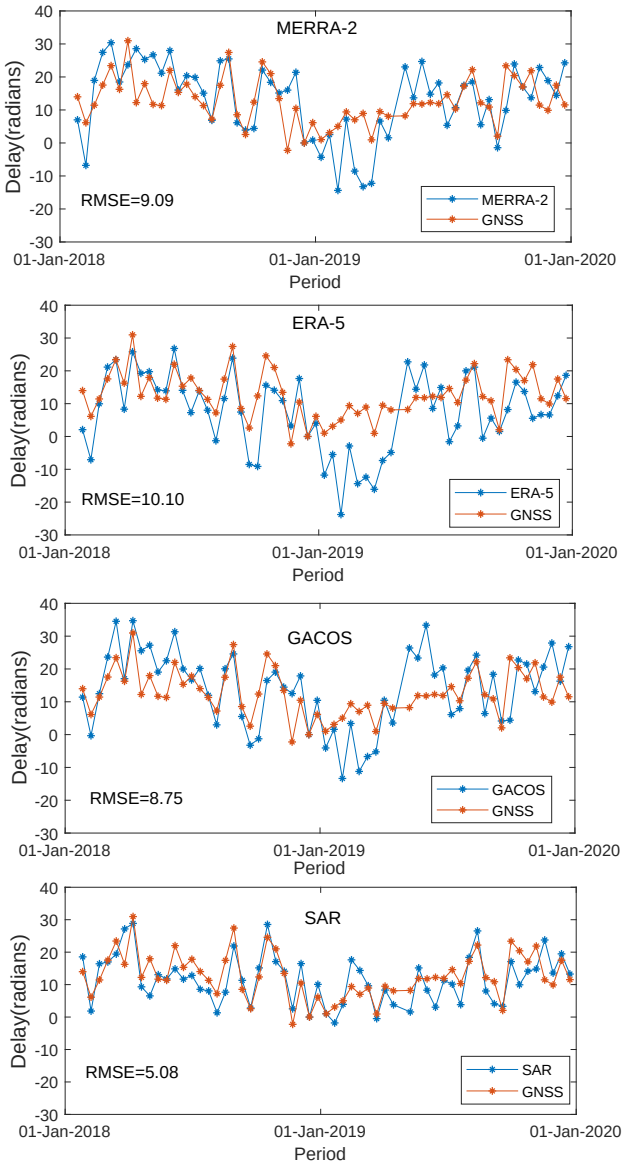

Figure 5. Time-series comparison of NWM tropospheric delays and SAR tropospheric delays with GNSS tropospheric delays at GNSS station KYN5. The tropospheric delays are referenced to GNSS station KYN7 and date 12-16-2018. .

NWM and GNSS delays was low. However, on some days, we observe a significant discrepancy as high as 30 rad. The large discrepancy can be attributed to the days in which the turbulent tropospheric delay was strong to which the NWM-based estimates failed to estimate owing to their spatial resolution. Among the three NWM-based tropospheric delays, GACOS had a better temporal fit with an RMSE value of 8.75 rad than ERA-5 and MERRA-5, which recorded RMSE values of 10.15 and 9.09, respectively. The different RMSE values among the three numerical weather models can be attributed to the differences

in the data resolution and interpolation methods. In comparison, we observe a good temporal fit between the SAR-based tropospheric delay estiamted in our approach and the GNSS tropospheric delay. Although we observed a discrepancy , it was not erratic as recorded in the NWM-based tropospheric delay estimates, such that their differential delay was still negligible. The differences in the estimates can be attributed to GNSS processing errors and different observation strategies between SAR and GNSS.

3.3 Comparison of different correction methods

Assuming that all other interferometric components have been accounted for, the phase change in short-interval interferograms can be attributed to tropospheric delay differences between the two SAR acquisition days. Therefore, correction of the tropospheric delay should lead to a significant decrease in the magnitude and spatial correlation of the unwrapped phase if the tropospheric delay correction method is effective. We observe

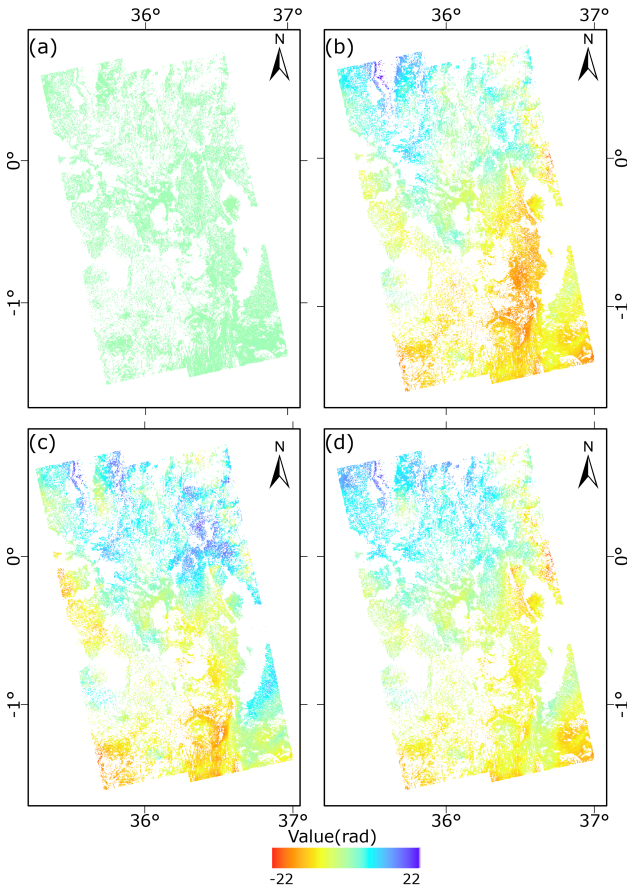

Figure 6. Example of a corrected interferogram (20190801-20190813) with different correction methods. In (a), the tropospheric delay is corrected using SAR-based estimates, whereas in (b), (c), and (d), corrections are performed using ERA-5, MERRA-2, and GACOS tropospheric delay estimates, respectively.

large residuals after correction using the three NMW-based estimates as shown in figure 6. The large residuals indicate that the NWM-based correction method does not significantly reduce tropospheric noise in the interferograms. The small residuals indicate that correction using SAR-based tropospheric delay estimates significantly reduces the spatial variability in the interferograms.

3.4 Performance assessment of the different correction techniques

We quantify the performance of the different correction methods by comparing the experimental variograms of the interferograms before and after applying the correction. We observe no

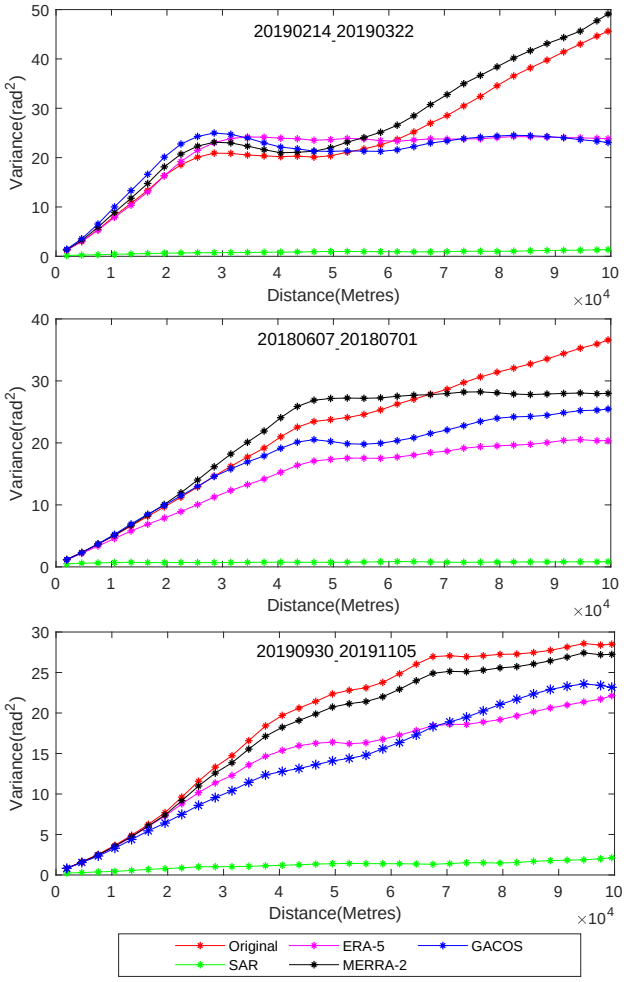

Figure 7. Evaluation of the tropospheric delay correction using experimental variograms showing spatial correlations before and after correction of short-interval interferograms using SAR-based and numerical weather model techniques.

significant change in the spatial correlation at short wavelengths using the three numerical weather models, as shown in figure 7, where no change in the shape of the variogram between the NWM-corrected variogram and the original interferogram is recorded. Similarly, a comparison of variances at a distance lag of 2000m shows no significant decrease in variances, as shown in figure 8, implying NWM-based tropospheric delay estimates have no impact on mitigation of turbulent delay. At longer wavelengths, we observe cases where the numerical weather models significantly reduces the tropospheric noise and cases of increased noise after correction, as listed in table 2. The increased variance after applying the correction indicates the limitation of NWM-based tropospheric delays in mitigating tropospheric noise in InSAR, and their potential to introduce more noise into the interferogram that affects the retrieval of time series displacement. Long-wavelength tropospheric variability is associated with stratified delays, which explains why numerical weather models can mitigate tropospheric delays to some

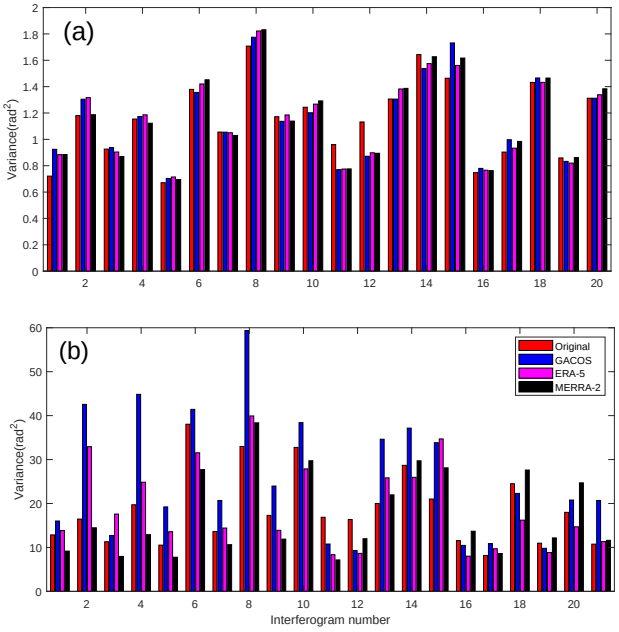

Figure 8. A comparison of the variances of the first 20 interferograms in the SBAS network in Appendix 1 before and after applying the correction using the NWM-based tropospheric delays . (a) shows the variances at lag distance 2000 m, while (b) shows the variance at lag distance 40000 m.

Table 2. Summary of changes in the variances of corrected interferograms at a distance lag of 40000m

Name	Decrease	Increase
ERA-5	78	93
MERRA-2	84	87
GACOS	110	61

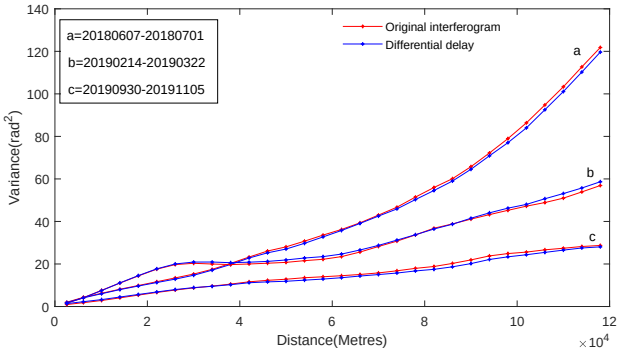

Figure 9. An example of spatial dependence between short interval interferograms and their corresponding SAR-based differential delay

extent. These wavelengths also correspond to the resolution of the SAR models; hence, the better performance of GACOS than those of ERA-5 and MERRA-2. However, their effectiveness in correcting tropospheric delay works under the strong assumption of elevation dependence of tropospheric delay variation in interferograms. In the presence of local tropospheric variability independent of elevation, the usability of correcting differential delay becomes minimal.

In contrast, we observed a significantly reduced spatial dependence at short and long wavelengths in all interferograms using the SAR-based estimated tropospheric delay. The SAR-based approach resulted in a significant decrease in spatial variability owing to the correct tropospheric delay estimation as shown in figure 7. In addition, the phase variability in short-interval interferograms is primarily attributed to changes in the tropospheric delay differences, as explained in Section 2. Hence, the differential delay and short-interval interferogram are expected to exhibit similar spatial variability if the tropospheric delay is correctly estimated. The similarity in the variogram shapes, as shown in figure 9, between the differential tropospheric delay and short-interval interferogram explains the significant reduction in the spatial correlation between the corrected interferogram and original interferograms.

4. CONCLUSION

The interplay of limited data to initialize numerical weather models, the coarse spatial resolution, and the assumption of topography dependence in tropospheric delay variability limits NWM-based tropospheric delay estimates for capturing the local tropospheric delay variability. Consequently, their use in mitigating short-wavelength turbulent delays is limited and they can only mitigate long-wavelength stratified delays in the presence of topography-correlated tropospheric delays. The increased variance at longer wavelengths after correction is associated with interpolation errors and the rapidly changing troposphere, which numerical weather models fail to capture. The increased variance at longer wavelengths after correction is associated with interpolation errors and the rapidly changing troposphere, which numerical weather models fail to capture. Thus, the observed significant differences in tropospheric delay estimates among the three NWMs and the large disparity on some days between the NWM-based tropospheric estimates and GNSS tropospheric delay estimates. The good temporal fit with GNSS tropospheric delay estimates demonstrates the capability of SAR-based tropospheric delay estimates to accurately capture tropospheric delay variability. This is further replicated by the similar spatial variability between short-interval and InSAR-based differential delays and the significant reduction in spatial correlation in interferograms after correction. Future work will focus on utilizing complementary numerical weather models and SAR-based tropospheric delays to mitigate tropospheric noise in the presence of rapid, large-amplitude deformation.

ACKNOWLEDGEMENTS

We thank DAAD through the Kenya-Germany postgraduate training program for funding this work. We acknowledge the ESA for Sentinel-1 data access; Sentinel 1 data were retrieved from the Alaska satellite facility (ASF DAAC). GNSS data were retrieved from the UNAVCO-distributed active archive data center.

REFERENCES

Amelung, F., Galloway, D. L., Bell, J. W., Zebker, H. A., Laczniak, R. J., 1999. Sensing the ups and downs of Las Vegas: InSAR reveals structural control of land subsidence and aquifer-system deformation. *Geology*, 27(6), 483–486.

Bekaert, D., Walters, R., Wright, T., Hooper, A., Parker, D., 2015. Statistical comparison of InSAR tropospheric correction techniques. *Remote Sensing of Environment*, 170, 40–47. doi.org/10.1016/j.rse.2015.08.035.

Castellazzi, P., Arroyo-Domínguez, N., Martel, R., Calderhead, A. I., Normand, J. C., Gárfias, J., Rivera, A., 2016. Land subsidence in major cities of Central Mexico: Interpreting InSAR-derived land subsidence mapping with hydrogeological data. *International Journal of Applied Earth Observation and Geoinformation*, 47, 102–111. doi.org/10.1016/j.jag.2015.12.002.

Elliott, J., Walters, R., England, P., Jackson, J., Li, Z., Parsons, B., 2010. Extension on the Tibetan plateau: recent normal faulting measured by InSAR and body wave seismology. *Geophysical Journal International*, 183(2), 503–535. doi.org/10.1111/j.1365-246X.2010.04754.x.

Fattahi, H., Agram, P., Simons, M., 2016. A network-based enhanced spectral diversity approach for TOPS time-series analysis. *IEEE Transactions on Geoscience and Remote Sensing*, 55(2), 777–786. doi: 10.1109/TGRS.2016.2614925.

Fattahi, H., Simons, M., Agram, P., 2017. InSAR time-series estimation of the ionospheric phase delay: An extension of the split range-spectrum technique. *IEEE Transactions on Geoscience and Remote Sensing*, 55(10), 5984–5996.

Ferretti, A., Prati, C., Rocca, F., 2001. Permanent scatterers in SAR interferometry. *IEEE Transactions on geoscience and remote sensing*, 39(1), 8–20. doi: 10.1109/36.898661.

Foster, J., Kealy, J., Cherubini, T., Businger, S., Lu, Z., Murphy, M., 2013. The utility of atmospheric analyses for the mitigation of artifacts in InSAR. *Journal of Geophysical Research: Solid Earth*, 118(2), 748–758. doi:10.1002/jgrb.50093.

Furuya, M., Satyabala, S., 2008. Slow earthquake in Afghanistan detected by InSAR. *Geophysical Research Letters*, 35(6. doi.org/10.1029/2007GL033049).

Golub, G. H., Hansen, P. C., O'Leary, D. P., 1999. Tikhonov regularization and total least squares. *SIAM journal on matrix analysis and applications*, 21(1), 185–194.

Hamling, I. J., Kilgour, G., 2021. Comment on the paper titled "Harvey, M., 2021. Sentinel-1 InSAR captures 2019 catastrophic White Island eruption. Journal of Volcanology and Geothermal Research. 411, https://doi.org/10.1016/j.jvolgeores.2020.107124". *Journal of Volcanology and Geothermal Research*, 420, 107234. doi.org/10.1016/j.jvolgeores.2021.107234.

Hanssen, R. F., 2001. *Radar interferometry: data interpretation and error analysis*. 2, Springer Science & Business Media.

Herring, T., King, R., McClusky, S. et al., 2010. Introduction to gamit/globk. *Massachusetts Institute of Technology, Cambridge, Massachusetts*.

Hooper, A., Bekaert, D., Spaans, K., Arıkan, M., 2012. Recent advances in SAR interferometry time series analysis for measuring crustal deformation. *Tectonophysics*, 514, 1–13.

Jolivet, R., Agram, P. S., Lin, N. Y., Simons, M., Doin, M.-P., Peltzer, G., Li, Z., 2014. Improving InSAR geodesy using global atmospheric models. *Journal of Geophysical Research: Solid Earth*, 119(3), 2324–2341.

Liang, C., Agram, P., Simons, M., Fielding, E. J., 2019. Ionospheric correction of InSAR time series analysis of C-band Sentinel-1 TOPS data. *IEEE Transactions on Geoscience and Remote Sensing*, 57(9), 6755–6773. doi: 10.1109/TGRS.2019.2908494.

Loibl, D., Bookhagen, B., Valade, S., Schneider, C., 2019. OSARIS, the "open source SAR investigation system" for automatized parallel InSAR processing of sentinel-1 time series data with special emphasis on cryosphere applications. *Frontiers in Earth Science*, 7, 172.

Morishita, Y., Lazecky, M., Wright, T. J., Weiss, J. R., Elliott, J. R., Hooper, A., 2020. LiCSBAS: an open-source InSAR time series analysis package integrated with the LiCSAR automated Sentinel-1 InSAR processor. *Remote Sensing*, 12(3), 424. doi:10.3390/rs12030424.

Murray, K. D., Bekaert, D. P., Lohman, R. B., 2019. Tropospheric corrections for InSAR: Statistical assessments and applications to the Central United States and Mexico. *Remote Sensing of Environment*, 232, 111326. doi.org/10.1016/j.rse.2019.111326.

Rosen, P. A., Gurrola, E. M., Agram, P., Cohen, J., Lavalle, M., Riel, B. V., Fattahi, H., Aivazis, M. A., Simons, M., Buckley, S. M., 2018. The insar scientific computing environment 3.0: a flexible framework for nisar operational and user-led science processing. *IGARSS 2018-2018 IEEE International Geoscience and Remote Sensing Symposium*, IEEE, 4897–4900. doi: 10.1109/IGARSS.2018.8517504.

Shen, L., Hooper, A., Elliott, J., 2019. A spatially varying scaling method for InSAR tropospheric corrections using a high-resolution weather model. *Journal of Geophysical Research: Solid Earth*, 124(4), 4051–4068. doi.org/10.1029/2018JB016189.

Smith, E. K., Weintraub, S., 1953. The constants in the equation for atmospheric refractive index at radio frequencies. *Proceedings of the IRE*, 41(8), 1035–1037.

Stephens, K. J., Wauthier, C., Bussard, R. C., Higgins, M., LaFemina, P. C., 2020. Assessment of mitigation strategies for tropospheric phase contributions to InSAR time-series datasets over two Nicaraguan volcanoes. *Remote Sensing*, 12(5), 782. doi.org/10.3390/rs12050782.

Ye, X., Kaufmann, H., Guo, X., 2004. Landslide monitoring in the Three Gorges area using D-InSAR and corner reflectors. *Photogrammetric Engineering & Remote Sensing*, 70(10), 1167–1172. doi.org/10.14358/PERS.70.10.1167.

Yip, S. T. H., Biggs, J., Albino, F., 2019. Reevaluating volcanic deformation using atmospheric corrections: implications for the magmatic system of Agung Volcano, Indonesia. *Geophysical Research Letters*, 46(23), 13704–13711. doi.org/10.1029/2019GL085233.

Yu, C., Li, Z., Penna, N. T., Crippa, P., 2018. Generic atmospheric correction model for Interferometric Synthetic Aperture Radar observations. *Journal of Geophysical Research: Solid Earth*, 123(10), 9202–9222. doi.org/10.1029/2017JB015305.

Yu, C., Penna, N. T., Li, Z., 2017. Generation of real-time mode high-resolution water vapor fields from GPS observations. *Journal of Geophysical Research: Atmospheres*, 122(3), 2008–2025. doi.org/10.1002/2016JD025753.

Yunjun, Z., Fattahi, H., Amelung, F., 2019. Small baseline InSAR time series analysis: Unwrapping error correction and noise reduction. *Computers & Geosciences*, 133, 104331. doi.org/10.1016/j.cageo.2019.104331.

Zhang, Y., Meng, X., Jordan, C., Novellino, A., Dijkstra, T., Chen, G., 2018. Investigating slow-moving landslides in the Zhouqu region of China using InSAR time series. *Landslides*, 15(7), 1299–1315. doi.org/10.1007/s10346-018-0954-8.

APPENDIX

SBAS network